# Application of Weak-Beam Dark-Field STEM for Dislocation Loop Analysis⋆

Yan-Ru Lin[1*], Yao Li[2,3], Steven J. Zinkle[1,2], Jose' D. Arregui-Mena[1], M. Grace Burke[1,4]

[1] *Materials Science and Technology Division, Oak Ridge National Laboratory, Oak Ridge, TN 37831 USA*

[2]*Department of Nuclear Engineering, University of Tennessee, Knoxville, TN 37996, USA*

[3]*Los Alamos National Laboratory, Los Alamos, NM 87545, USA*

[4]*Idaho National Laboratory, Idaho Falls, ID 83415, USA*

*Corresponding author

Postal Address: Oak Ridge National Laboratory, P.O. Box 2008, MS6136, Oak Ridge, TN 37831

Email: liny@ornl.gov

Co-author email addresses in order of appearance:

yli166@vols.utk.edu; szinkle@utk.edu; arreguimenjd@ornl.gov; unocicrr@ornl.gov; mary.burke@inl.gov

**Declaration of Competing Interest**:

None.

**Abstract**

Nanoscale dislocation loops formed by irradiation can significantly contribute to both irradiation hardening and embrittlement of materials when subjected to extreme nuclear reactor environments. This study explores the application of scanning transmission electron microscopy (STEM) – weak-beam dark-field (WBDF) methods for quantitative irradiation-induced defect analysis in crystalline materials, with a specific focus on dislocation loop imaging and analysis. A high-purity Fe-5 wt.%Cr model alloy was irradiated with 8 MeV $Fe^{2+}$ ions at 450°C to a fluence of $8.8\times10^{19}$ $m^{-2}$, inducing dislocation loops for analysis. While transmission electron microscopy (TEM) has traditionally been the primary tool for dislocation imaging, recent advancements in STEM technology have reignited interest in using STEM for defect imaging. This study introduces and compares three STEM-WBDF methods, demonstrating their effectiveness in suppressing background contrasts, isolating defect information for dislocation loop type classification, providing finer dislocation line images for small loop analysis, and presenting inside-outside contrast for identifying loop nature. Experimental findings indicate that STEM-WBDF methods surpass traditional TEM approaches, yielding clearer and more detailed images of dislocation loops. The study concludes by discussing the potential applications of STEM-WBDF techniques in defect analysis, emphasizing their adaptability across various material systems beyond nuclear materials.

**Keywords:** Dislocation; STEM; Weak beam dark field; Dislocation loops; Irradiation-induced defects, TEM

## 1 Introduction

Understanding the mechanical properties of crystalline materials relies heavily on using transmission electron microscopy (TEM) to characterize dislocations (Hirsch & Whelan, 1960; Howie, et al., 1962), which are among the most important defects in engineering materials for structural applications. Recent studies (Phillips, et al., 2011a; Phillips, et al., 2011b) have shown that conventional $g \cdot b$ invisibility criteria for dislocation imaging in diffraction contrast TEM are applicable in scanning transmission electron microscopy (STEM) when the experimental setting is appropriate, offering specific advantages. These advantages include a higher signal-to-noise ratio and reduced thickness fringes, bend contours, and other dynamical contrast effects. In nuclear material research, irradiation can induce dislocation loop formation (Lin, et al., 2021), which can be visualized using the same $g \cdot b$ invisibility criteria applied to dislocations (Yao, et al., 2013). Investigating dislocations and dislocation loops in irradiated materials is crucial for understanding the effects of irradiation on material properties and evaluating a material's lifetime in extreme nuclear reactor environments (Zinkle, 2020).

Recent advancements in STEM (Liu, 2021), including spherical aberration correction and the development of direct electron and pixelated STEM detectors, have renewed interest in STEM imaging of dislocations and irradiation-induced defects (e.g., cavities, stacking faults, and point defect clusters) (Fung, et al., 2018; Lin, et al., 2014; Parish, et al., 2015). Although TEM methods have traditionally dominated dislocation imaging, STEM using convergent beams emerged as a promising alternative as early as the 1970s (Maher & Joy, 1976). Apart from dislocation contrast, diffraction of the electron beam introduces additional dynamical contrast such as bend contours and thickness fringes (Heidenreich, 2004). These can complicate image contrast, potentially obscuring the finer details of dislocations, dislocation loops, or other

microstructures/defects under TEM operating conditions. To deal with this unfavorable situation, STEM methods for imaging dislocations with suppressed background contrasts due to dynamical diffraction effects were proposed. This takes advantage of the oscillation of the electron beam in STEM mode, which can significantly cancel out dynamical diffraction contrasts when the size of the convergence semi-angle (α) and the collection angle (β) are well arranged (Zhu, et al., 2018). A "clean background" free of dynamical diffraction effects is especially crucial for analyzing defects and microstructures in irradiated materials. Irradiation-induced defects, like dislocation loops or cavities, can be as small as 1 nm—much smaller than the length of dislocation lines, which can extend thousands of nanometers. Additionally, when using focused ion beam (FIB) methods to prepare TEM samples, FIB damages can produce "black dot" or "black spot" defects, complicating differentiation from very fine irradiation-induced loops (Zhong, et al., 2022). Recent studies demonstrated that the flash electropolishing method minimizes this artifact by removing the thin layer with FIB damage from FIB-produced TEM samples of steel or other alloys (Li, et al., 2023).

Dislocation loops play a significant role in irradiation hardening and embrittlement of materials at low-to-intermediate temperatures, making their analysis central to understanding the materials' response to irradiation (Klueh, et al., 2008). Traditionally, determining the Burgers vector of a loop involves imaging with at least two non-collinear g vectors, a time-consuming process requiring sample tilting. Yao et al. (Yao, et al., 2013) introduced a efficient method in TEM mode, based on the projected loop orientation and features (e.g., edge-on, plan-view, or elliptical loops) at specific zone axes, to determine loop types (e.g., ½ ⟨111⟩ or ⟨100⟩ loops) in irradiated BCC Fe-based steels. This method was later extended to STEM mode by researchers (Parish, et al., 2015; Xiu, et al., 2021) for examining dislocation loops in BCC and FCC

materials under certain zone axes. However, these methods have limitations when the loop diameter is less than 5-10 nm. When the thickness of the loop's contour line is similar to the loop size, the loop appears as a “black dot” loop for every type of loop. This makes it impossible to preserve the crystallographic information of these loops for on-zone imaging in both TEM and STEM modes.

To address these gaps, this study focuses on applying various STEM methods for dislocation loop imaging, and comparing them to traditional TEM methods. Although previous studies have demonstrated the value of bright-field (BF) STEM over traditional TEM methods (Parish, et al., 2015; Wang & Bentley, 1991; Xiu, et al., 2021), our current investigation uniquely focuses on the advantages of weak-beam dark-field (WBDF) STEM. We outline steps for establishing WBDF conditions for dislocation loop imaging in STEM mode and discuss the advantages of using WBDF-STEM for dislocation and dislocation loop analysis. The proposed approach involves using the WBDF-STEM method to capture finer details of dislocation loops and determine their Burgers vector and nature (e.g., interstitial or vacancy type). Furthermore, this method proves particularly beneficial in accurately locating dislocation line and loop cores, especially in situations involving bent samples, small black dot loops, or crowded defects. Importantly, this approach extends beyond irradiated materials, offering a versatile method for defect analysis in other material systems.

## 2 Materials and Methods

### 2.1 Sample preparation

The study employed a body-centered-cubic (BCC) high-purity Fe-5 wt.%Cr model alloy. To induce dense dislocation loops, the Fe-5Cr samples underwent irradiation with 8 MeV $Fe^{2+}$ ions (with an ion range of ~2 μm) at 450°C at the Michigan Ion Beam Laboratory (MIBL) to a

total fluence of $8.8\times10^{19}$ $m^{-2}$ (equivalent to doses of ~3.7 dpa at midrange, ~1 μm). Details of the material and irradiation experiments can be found elsewhere (Zhu, et al., 2024). Prior to the FIB lift-out process for TEM sample preparation, a Zeiss EVO SEM equipped with an electron backscatter diffraction (EBSD) detector was used to identify grains with a surface plane {100} and a normal close to the ⟨100⟩ zone axes. Subsequently, TEM samples were prepared using a Zeiss Auriga SEM-FIB, employing a 30kV Ga probe throughout the FIB process with ion beam currents ranging from 12 nA to 50 pA. The flash electropolishing method, as reported in a previous study (Yao, et al., 2013), was applied to remove FIB-induced damages from the TEM foil surfaces. All TEM sample preparations were conducted at the Institute for Advanced Materials & Manufacturing (IAAM) lab at the University of Tennessee, Knoxville. TEM and STEM analyses were performed using a JEOL 2100F operated at 200kV, located at the Low Activation Materials Development and Analysis (LAMDA) laboratory at Oak Ridge National Laboratory.

## 2.2 TEM and STEM imaging conditions

The distribution of dislocation loops is shown in the STEM images of the ion-irradiated Fe-5Cr cross-section sample, where the ion beam had been injected perpendicular to the surface (top of Figs. 1a and 1b). In BCC Fe systems, ion irradiation can induce ½ ⟨111⟩{111} and ⟨100⟩ {100} dislocation loops, as schematically shown in Figs. 1d and c. For ion irradiation of a {100} surface with the [100] zone axis, ½ ⟨111⟩ elliptical loops align either parallel to [011] or [01$\bar{1}$]. Conversely, [001] and [010] loops exhibit an edge-on orientation, with [001] loops perpendicular to [002] and [010] loops perpendicular to [020]. Finally, [100] loops are visible as plan-view loops. In general, ⟨100⟩ loops in irradiated Fe-Cr alloys dominate at elevated temperatures (Yao, et al., 2010), in agreement with the STEM bright-field (BF) and annular

dark-field (ADF) images in Figs. 1a and 1b, respectively. All STEM images in this study were captured at a camera length of 8 cm, STEM convergence angle of 4 or 13 mrad, BF detector collecting angles from 0-11 mrad, and the ADF detector collecting angles from 19-42 mrad. Setting up STEM-WBDF imaging conditions involved using the objective (OL) aperture to select the desired diffraction disk, as depicted in Fig. 1f.

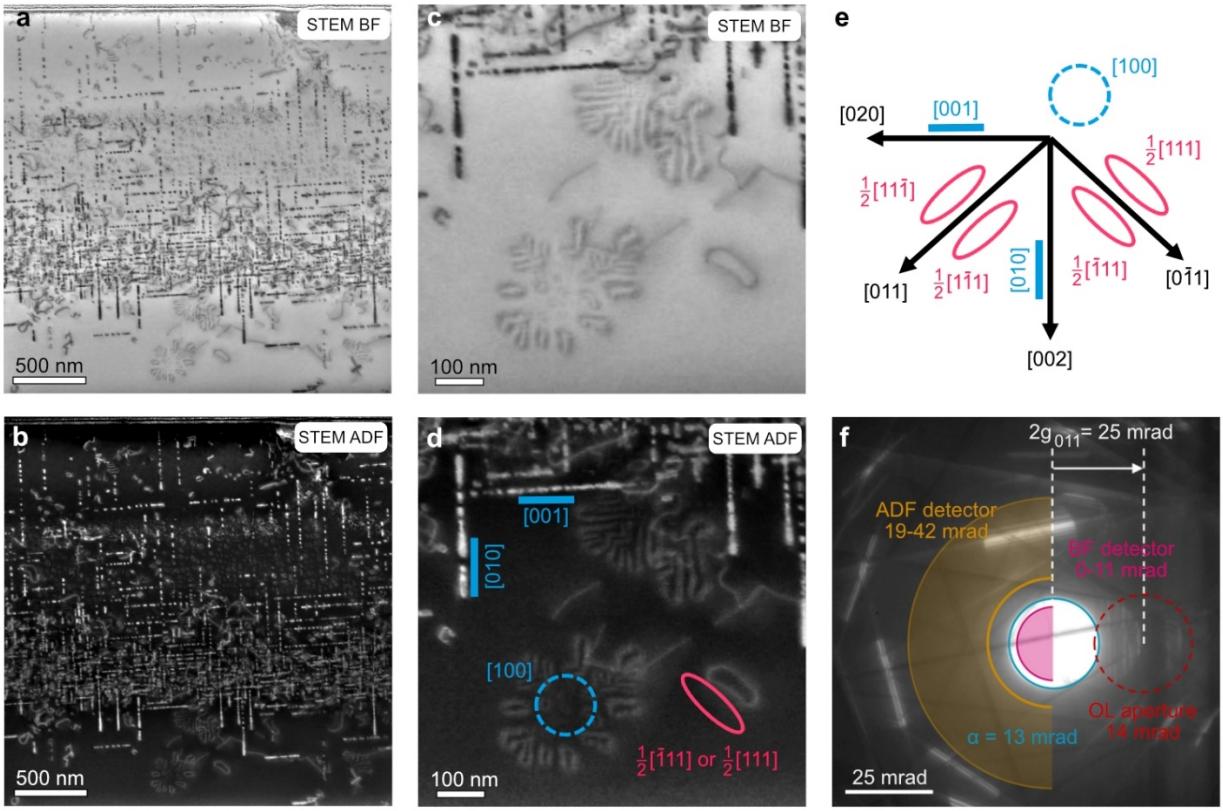


**Fig 1.** STEM imaging conditions for dislocation loops in ion irradiated Fe-5Cr: (a, c) STEM-BF and (b, d) STEM-ADF micrographs acquired along the [100] zone axis with an 8 cm camera length. (e) Schematic diagram illustrating the projected loop types along the [100] zone axis, corresponding to the crystal orientation in Fig. 1d. ½ ⟨111⟩ elliptical loops are depicted in red, while ⟨100⟩ loops are in blue. (f) Illustration of the size and collection angles of the BF and ADF detectors, as well as the OL aperture (BF: bright-field, ADF: annular dark-field, OL: objective).

To optimize the suppression of dynamical background contrasts in STEM images for the JEOL 2100F, we tested the 70 µm, 50 µm, and 10 µm condenser (CL) apertures with a fixed camera length of 8 cm, imaging the same area of interest (Fig. 2). For TEM imaging, the 70 µm

condenser aperture was used. In Figs. 2b-d, the convergent beam electron diffraction (CBED) patterns clearly demonstrate a decrease in diffraction disc size with decreasing condenser aperture sizes. The corresponding incident angles (α) are labeled on the lower left of the CBED patterns. Overall, STEM images (Figs. 2 f-h) exhibited superior suppression of background contrast compared to the TEM image (Fig. 2e). Among the STEM imaging conditions, the 50 µm CL aperture with an intermediate size produced the best STEM-BF image with suppressed background contrast (Fig. 2g). This supports the previous study by Zhu *et al.* indicating that Kossel-Mollenstedt (K-M) fringes can largely "cancel out" when the α angle is reasonably large, and the β angle is comparable to the α angle (Zhu, et al., 2018). However, for STEM-WBDF methods, the diffraction disc in the CBED patterns needs to be separated to isolate the diffraction signal. Therefore, in this study, the 10 µm CL aperture was used for STEM-WBDF imaging (Fig. 2d).

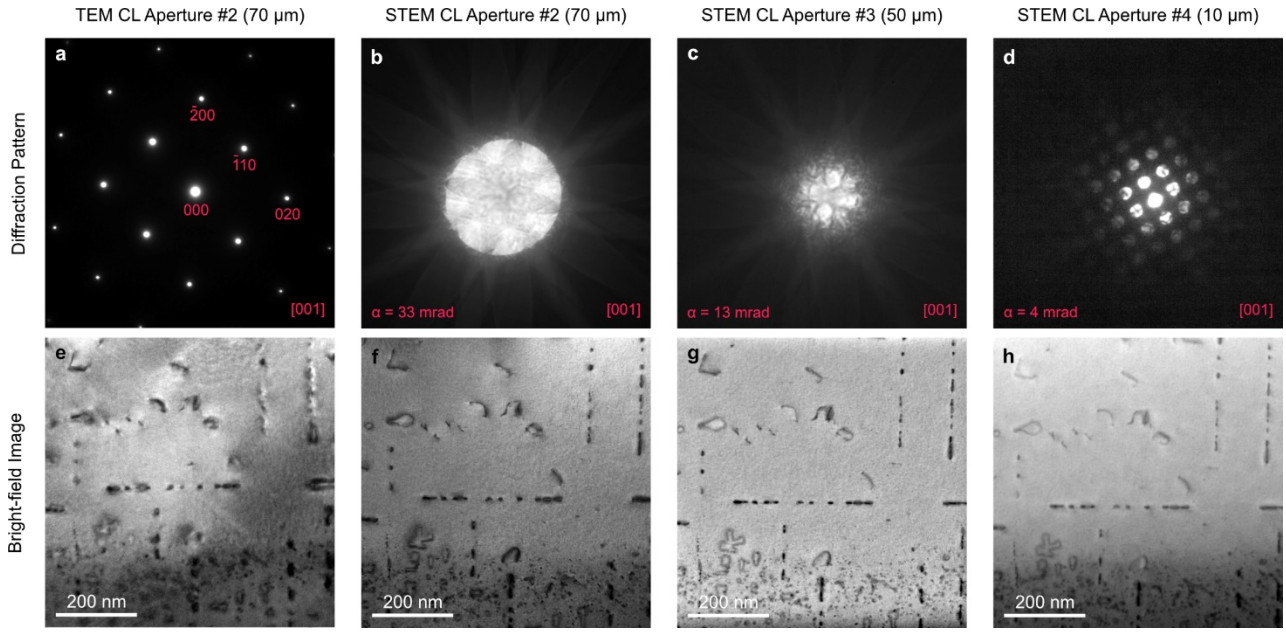


**Fig 2.** Comparison of background contrast in TEM and STEM modes with varying condenser (CL) aperture sizes ranging from 10 to 70 µm: (a) selected area electron diffraction (SAED) pattern in TEM mode from

Fig. 2e. (b-d) convergent beam electron diffraction (CBED) patterns from Figs. 2f-h. (e) TEM-BF image. (f-h) STEM-BF images. All images were captured in the identical area along the [001] zone axis.

In this study, we compared three STEM-WBDF methods, two from previous studies (Iwata & Saka, 2017; Miao, et al., 2018) and one newly proposed herein. The detailed steps for setting up STEM-WBDF conditions are summarized in Table 1 and Figs. 3 b-d. Method 1, akin to the conventional WBDF setup in TEM mode, involved exciting the 3g diffraction vector and detecting the transmitted beam on the BF detector and one diffracted beam on the ADF detector, with an objective aperture used to filter out information from other diffraction signals. Method 2 utilized a shifted convergent beam electron diffraction (CBED) pattern via the projector system, moving the g disc to the BF detector, which functioned as both a signal collector and an "aperture." In Method 3, the sample was tilted to the standard two-beam condition by exciting the g beam with an excitation error near zero, and a proper objective aperture was inserted to allow only the -g beam to be detected on the ADF detector.

**Table 1.** Procedures for acquiring WBDF images in TEM and STEM modes.

| | TEM | STEM method 1 (Miao, et al., 2018) | STEM method 2 (Iwata & Saka, 2017) | STEM method 3 |
|---|---|---|---|---|
| Step 1 | Tilt the sample to satisfy Bragg condition for g | Tilt the sample to satisfy Bragg condition for 3g | Tilt the sample to satisfy Bragg condition for 3g | Tilt the sample to satisfy Bragg condition for g |
| Step 2 | Deflect the direct-beam (T) beam to –g (Now Bragg condition for 3g is satisfied) | Set camera length long enough to separate the CBED discs | Set camera length long enough to separate the CBED discs | Set camera length long enough to separate the CBED discs |
| Step 3 | Insert an objective aperture to cover g | Insert an objective aperture to cover g | Bring the g disc to the center of the detector by deflector of the projector lens | Insert an objective aperture to cover -g |
| Step 4 | Record the image | Record the image by STEM-ADF detector | Record the image by STEM-BF detector | Record the image by STEM-ADF detector |

## 3 Results

Fig. 3 shows a compilation of BF and WBDF micrographs of dislocation loops in irradiated Fe-5Cr through diverse TEM and STEM methods, as outlined in Table 1 and illustrated in Figs. 3a-d. All images are recorded from the identical region of the TEM foil to enable a direct comparison of contrast variations. The cropped SAED and CBED patterns in the lower right of each micrograph indicate the positions of the optic axis, direct beam (T), diffraction beam ($g = [011]$), detector (BF or ADF), and OL aperture. In TEM-BF (Fig. 3e) and TEM-WBDF (Fig. 3i) micrographs, discernible thickness fringes and background contrasts are evident. It was noted that all BF and WBDF micrographs obtained through the three STEM methods exhibited a suppression of thickness fringes (Fig. 3). Notably, the contrast of the images using STEM Method 2 was inverted between detectors; that is, ADF images were obtained using the BF detector (Fig. 3g) and BF images were obtaining using the ADF detector (Fig. 3k).

Furthermore, in Fig. 3k, the dislocation loops in the upper half of the image display dark contrast, whereas in the lower half, the loops exhibit white contrast. Lastly, in the comparison between STEM method 1 and method 3, the results were generally aligned, with minor differences in contrast intensity and the thickness of the loop's contour line.

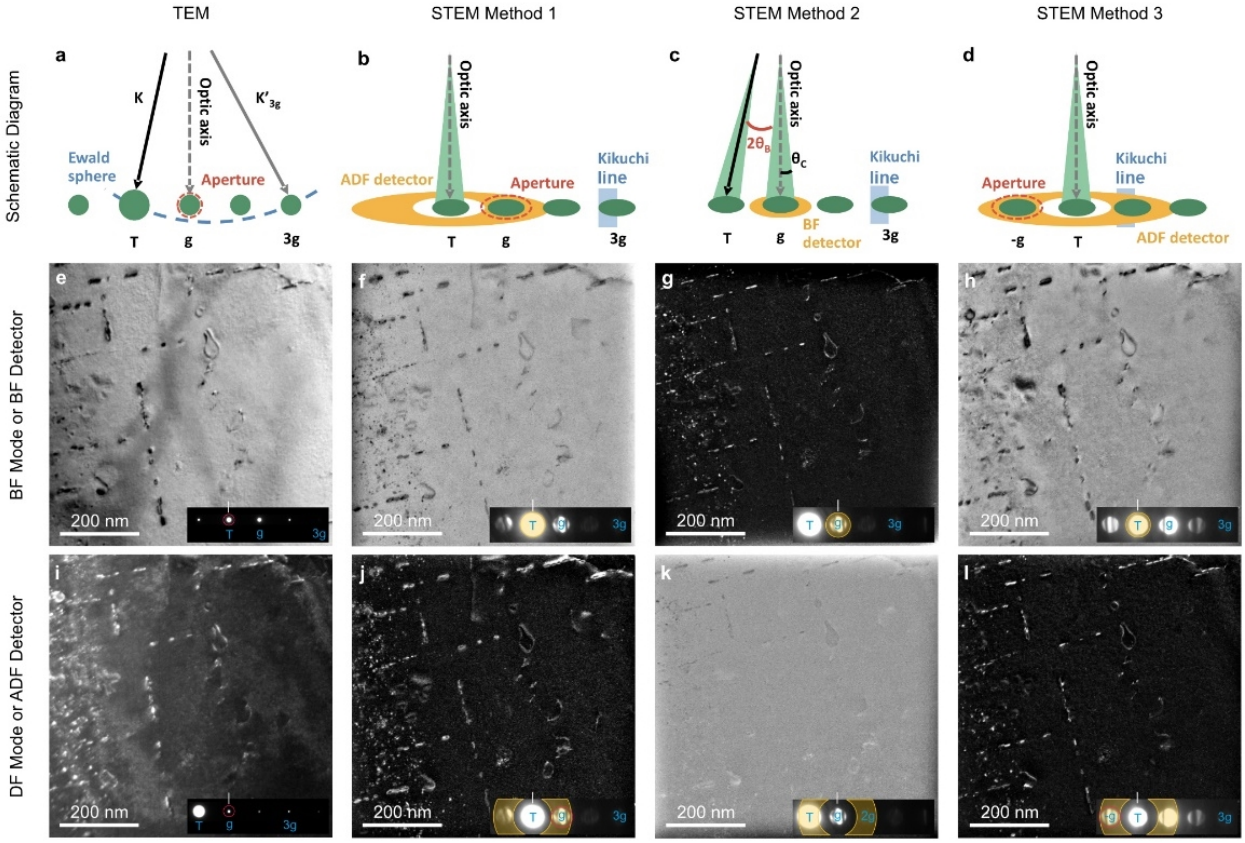


**Fig 3.** Collection of Bright-Field (BF) and Weak-Beam Dark-Field (WBDF) micrographs of dislocation loops in irradiated Fe-5Cr, captured through various TEM and STEM techniques: (a-d) schematic diagram illustrating the imaging conditions; (e) TEM-BF and (i) TEM-WBDF micrographs (column 1); (f) STEM-BF and (j) STEM-WBDF micrographs using STEM Method 1 (column 2); (g) STEM-BF and (k) STEM-WBDF micrographs using STEM Method 2 (column 3); (h) STEM-BF and (l) STEM-WBDF micrographs using STEM Method 3 (column 4). T is the direct beam and g is the diffraction beam with g=011.

As summarized in Table 2, identifying loop types necessitates a minimum of two non-colinear diffraction vectors with $g \cdot b = 0$. This is because, in three-dimensional space, a vector is determined by the cross product of two non-colinear vectors. To investigate whether the classic $g \cdot b$ invisibility criteria in TEM-WBDF condition is applicable to STEM-WBDF methods,

we focused on a higher-magnification area, tilting the sample along different g vectors to verify the appearance of distinct types of loops (Table 2). In Fig. 4, all the images were taken near or along the [100] zone axis. Figs. 4a and 4e are the STEM-BF and STEM-ADF images acquired in the on-zone condition, respectively. Consistent with previous on-zone STEM studies (Parish, et al., 2015; Xiu, et al., 2021), all types of dislocation loops were visible along the [100] zone axis. Edge-on defects corresponded to vertical [010] or horizontal [001] dislocation loop types, small plan-view loops were [100] loops, and several ½ ⟨111⟩ elliptical loops were also evident. When tilting the sample towards the $g = [002]$ direction to set up the (g, 3g) weak-beam condition without an objective aperture on the g diffraction disc (Figs. 4b and 4f), vertical [010] loops, which should not be present according to the $g[002] \cdot b[010] = 0$ criteria, still exhibited loop contrast with reduced intensity. After inserting an appropriately-sized objective aperture covering only the g diffraction disc, the vertical [010] loops in STEM-WBDF images were eliminated, as indicated by the green box in Fig. 4g. The plan-view [100] loops, marked by the blue box in Fig. 4g, also vanished following the $g[002] \cdot b[100] = 0$ criteria. Additionally, no signal was detected by the BF detector when the objective aperture was inserted and appropriately covered the g diffraction disc, as shown in Fig. 4c. Similar results were observed when tilting the sample toward the $g = [011]$ direction, impacting the ½ ⟨111⟩ loop contrast, as marked by the yellow box in Fig. 4h.

**Table 2.** The dot product calculation involving all seven Burgers vectors and diffraction vectors under the major zone axes in the BCC iron system.

| Zone | g\b | 111 | $11\bar{1}$ | $1\bar{1}1$ | $\bar{1}11$ | 100 | 010 | 001 |
|---|---|---|---|---|---|---|---|---|
| 001 | 200 | 2 | 2 | 2 | -2 | 2 | 0 | 0 |
| | 020 | 2 | 2 | -2 | 2 | 0 | 2 | 0 |

| | | | | | | | | |
|---|---|---|---|---|---|---|---|---|
| | 110 | 2 | 2 | 0 | 0 | 1 | 1 | 0 |
| | $1\bar{1}0$ | 0 | 0 | 2 | -2 | 1 | -1 | 0 |
| 011 | 200 | 2 | 2 | 2 | -2 | 2 | 0 | 0 |
| | $2\bar{1}1$ | 2 | 0 | 4 | -2 | 2 | -1 | 1 |
| | $0\bar{1}1$ | 0 | -2 | 2 | 0 | 0 | -1 | 1 |
| | $\bar{2}\bar{1}1$ | -2 | -4 | 0 | 2 | -2 | -1 | 1 |
| | $\bar{1}01$ | 0 | -2 | 0 | 2 | -1 | 0 | 1 |
| 111 | $\bar{2}11$ | 0 | -2 | -2 | 4 | -2 | 1 | 1 |
| | $1\bar{1}0$ | 0 | 0 | 2 | -2 | 1 | -1 | 0 |
| | $1\bar{2}1$ | 0 | 2 | -4 | 2 | -1 | 2 | -1 |
| | $0\bar{1}1$ | 0 | -2 | 2 | 0 | 0 | -1 | 1 |
| | $11\bar{2}$ | 0 | 4 | -2 | -2 | 1 | 1 | -2 |

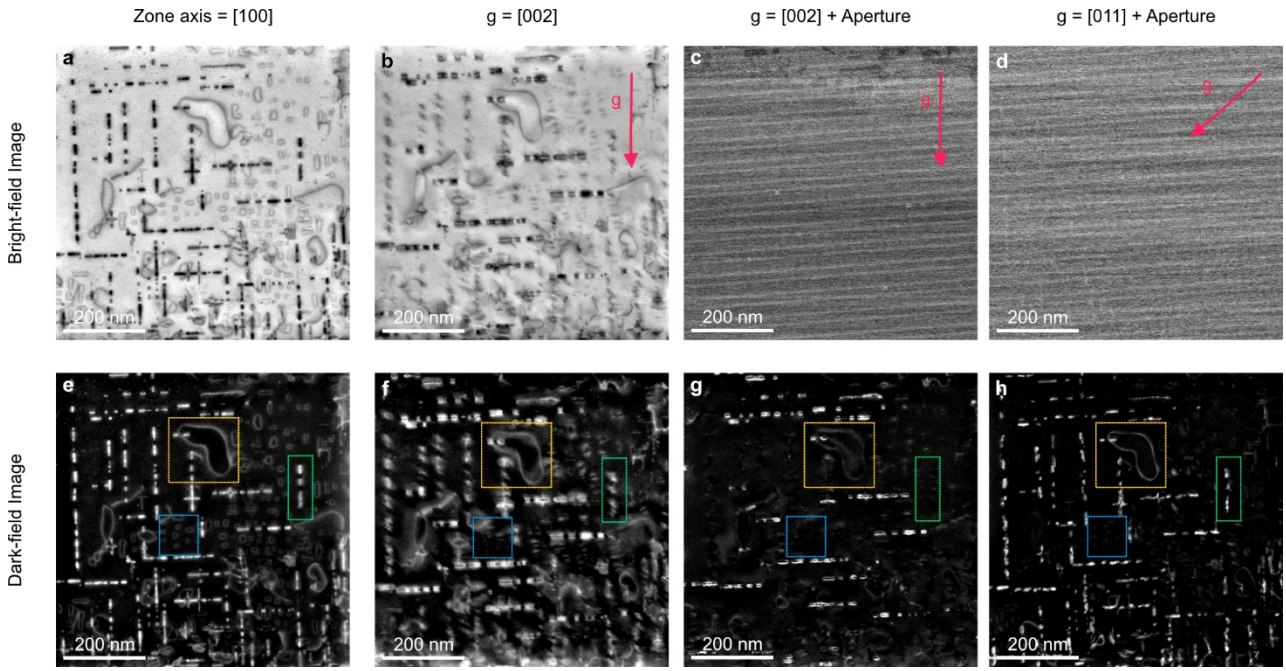

**Fig 4.** Appearance of dislocation loops imaged under various g vectors with and without objective apertures: (a-d) images recorded using the STEM-BF detector and (e-h) STEM-ADF detector. Images were acquired on-zone, weak-beam $g = [002]$ without an objective aperture, and weak-beam $g = [002]$ and $[011]$ with an objective aperture. The zone axis was near or along $[100]$.

A critical aspect of dislocation loop analysis involves determining their nature, whether interstitial or vacancy type. Traditionally, loop nature analysis depended on the inside-outside contrast technique (Jenkins, 1994), which can be challenging when dealing with complicated background contrast and small dislocation loops. Fig. 5 clearly demonstrates that STEM-WBDF images can reveal the inside-outside contrast of the small edge-on dislocation loops under diffraction conditions $g = [011]$ or $[\overline{011}]$ with $s_g > 0$. Fig. 5 also shows that the $[010]$ and $[001]$ edge-on dislocation loops appear as loop strings aligned along the $\langle 001 \rangle$ planes, rather than forming a single large dislocation loop. Similar observations were evident in plan-view $[100]$ loops, exemplified by the "flower shape" loop near the bottom of Figs. 1a and 1b.

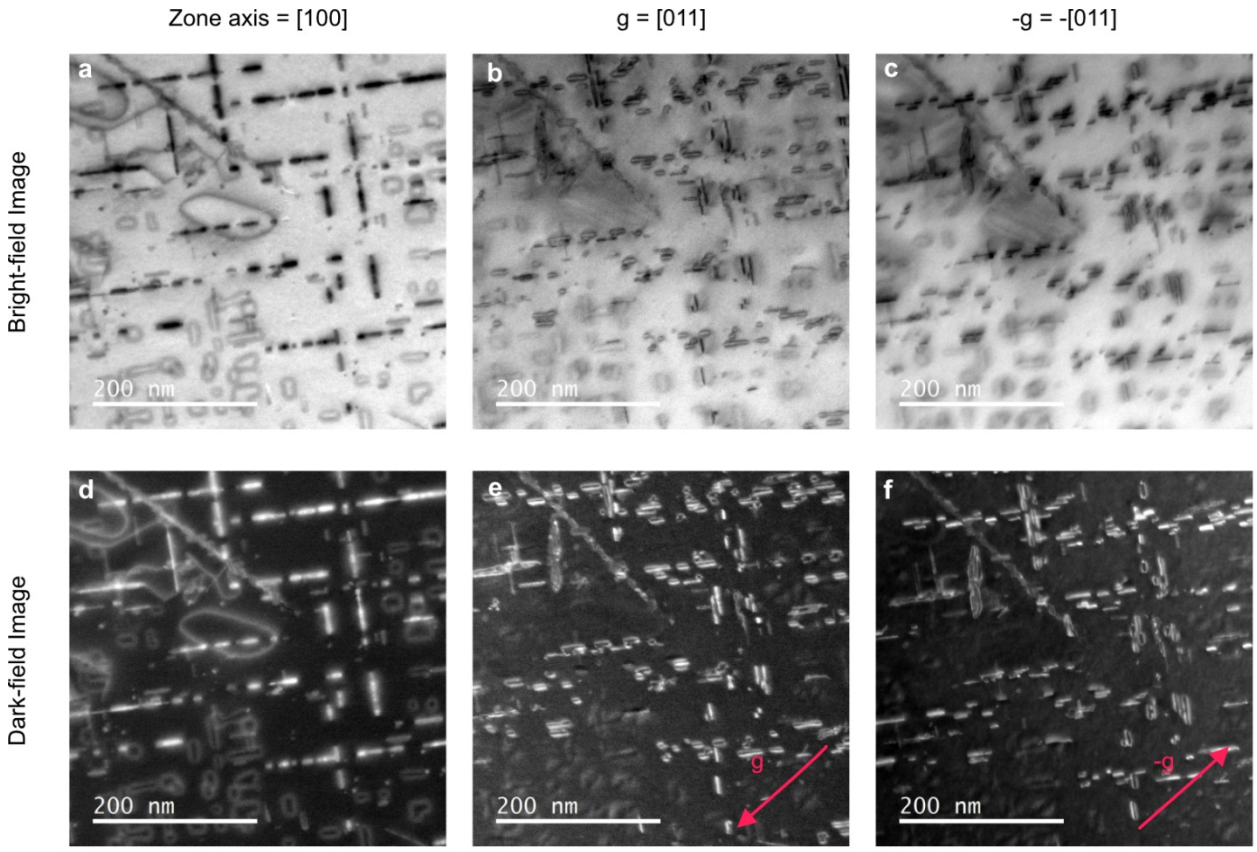


**Fig 5.** STEM on-zone and WBDF images demonstrating the inside-outside contrast of dislocation loops: (a-c) STEM-BF images, and (d-f) STEM-ADF. The orientation of the g vector is indicated by the pink arrow.

To evaluate the applicability of the inside-outside contrast mechanism with STEM-WBDF methods, a specific ½ ⟨111⟩ loop was examined by both TEM and STEM with the same imaging condition (Fig. 6). Although the STEM-WBDF image exhibited a cleaner background contrast and stronger loop contrast compared to the TEM-WBDF images, both TEM-WBDF and STEM-WBDF images of the loop indicated by the yellow dashed-lines in Fig. 6 displayed outside contrast when $g = [011]$ and inside contrast when $g = [\overline{011}]$. Following Föll's convention (Föll & Wilkens, 1975), the loop nature was determined to be of the interstitial type. In the ion-irradiated Fe-5Cr sample, nearly all of the dislocation loops were observed to be interstitial type, in agreement with expectations from prior studies on irradiated Fe alloys (Chen,

et al., 2016; Haley, et al., 2017). It is noted that in BCC Fe systems, irradiation-induced loops are assumed to be perfect loops, obviating the need to consider reverse inside-outside behavior for specific orientations. This demonstrates that the inside-outside contrast technique can be effectively combined with the STEM-WBDF method, providing better image quality for accurately determining the dislocation loop nature.

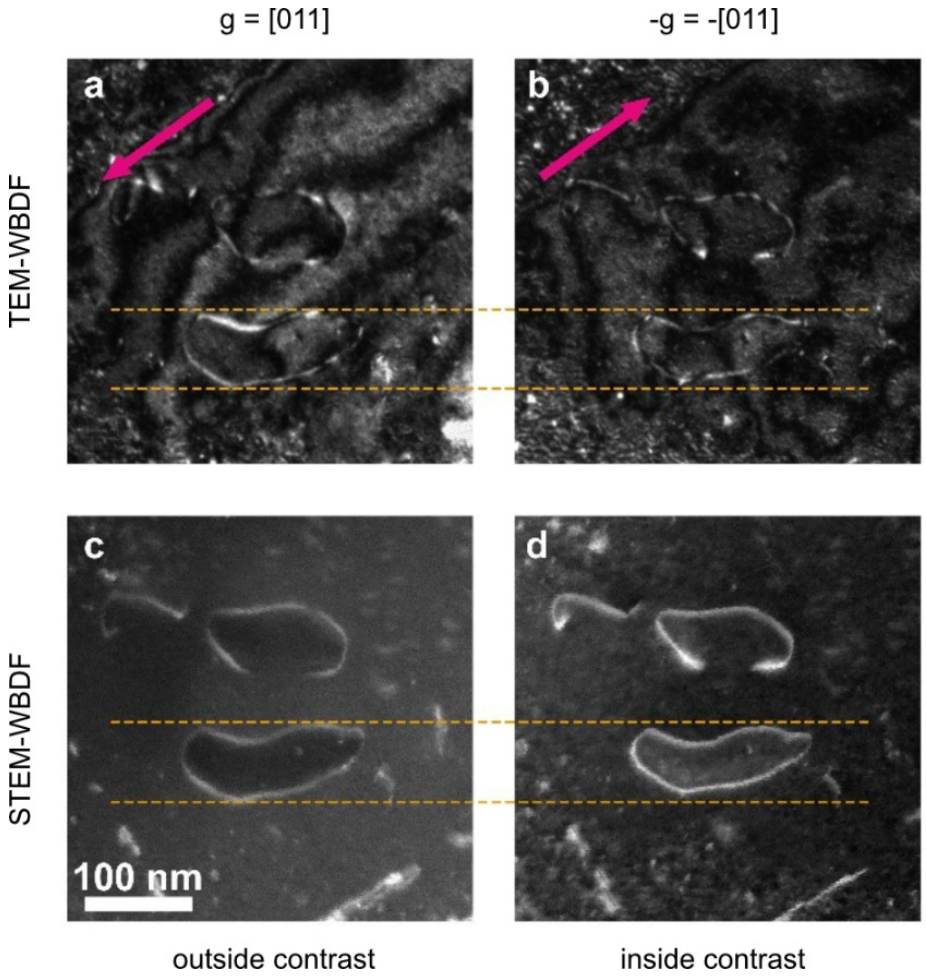


**Fig 6.** TEM and STEM WBDF images demonstrated the inside-outside contrast of an ½ ⟨111⟩ interstitial dislocation loop, indicated by the yellow-dashed lines: TEM-WBDF images with (a) $g = [011]$ and (b) $g = [0\bar{1}\bar{1}]$; STEM-WBDF images with (a) $g = [011]$ and (b) $g = [0\bar{1}\bar{1}]$. The zone axis was near $[100]$.

## 4 Discussion

### 4.1 Isolating Information on the Type and Nature of Dislocation Loops

In the early development of STEM defect imaging, the theory relied on the principle of reciprocity (Humphreys, 1981), where $\alpha_s = \beta_c$ and $\alpha_c = \beta_s$, with $\alpha$, $\beta$, $c$, and $s$ denoting incident angle, collection angle, TEM, and STEM, respectively. To optimize STEM advantages, such as smearing out thickness fringes and bending contours, a condition of $\beta_s$ being larger than $\alpha_c$ is desirable. Previous studies (Maher & Joy, 1976; Phillips, et al., 2011b) demonstrated that for fine details of defects to be visible in STEM images, it is essential to have $\beta_s \approx 10\alpha_c$. Precise control of the $\alpha_c$-to-$\beta_s$ ratio, achieved by adjusting the camera length and condenser aperture size, enabled defect micrographs in STEM mode with suppressed thickness fringes and bending contours to be obtained (Zhu, et al., 2018). However, setting up the optimal STEM-WBDF imaging condition with background-suppressed (suppression of dynamical contrast effect in the matrix) images requires consideration of the best combination of camera length, CL aperture size, OL aperture size, and collection angles for BF/ADF detectors, which may vary between microscopes and different materials or g vectors. In Fig. 2, although the 50 μm CL aperture showed the best background-suppressed STEM-BF images (Fig. 2g), the diffraction discs were too large and overlapped for BCC Fe along the [100] zone axis (Fig. 2c), thus making it challenging to set up the STEM-WBDF condition because the diffraction discs overlapped. A possible solution was to use a smaller CL aperture, slightly sacrificing background contrast suppression, as demonstrated in this study with the smaller 10 μm CL aperture (Fig. 2d) in the JEOL 2100 for STEM-WBDF setting. Another potential solution can involve the careful use of the JEOL "free lens control" that permits users to adjust the convergence angle for a given condenser aperture.

According to electron diffraction theory (Hirsch & Whelan, 1960), the half-width of a TEM-imaged dislocation line is approximately ~$\xi_g$ /3 (where $\xi_g$ is the extinction distance) under

a two-beam approximation with vector g excited, typically around ~10 nm. Consequently, determining the dislocation loop type solely with on-zone STEM-BF images may be challenging when the loop diameter is less than ~10 nm, making them appear as tiny “black dot” defects. Moreover, unlike the model alloys used in this study for fundamental research, nuclear materials typically comprise complex material systems in which dislocation loops can coexist with primitive dislocation lines, precipitates, and other irradiation-induced defects. For instance, it is common to observe dislocation loops nucleating around preexisting dislocations (Hernández-Mayoral, et al., 2016; Wen, et al., 2005). When different features overlap in the TEM/STEM projected images, this complexity poses a challenge in identifying and quantifying the loop type based on loop morphology and orientation in on-zone STEM images (Xiu, et al., 2021). Hence, employing STEM-WBDF methods for dislocation loop analysis is beneficial for isolating information on the type and nature of dislocation loops by tilting the sample to different g vectors.

It is worth noting that an appropriate setup, including the use of an objective aperture, is necessary to obtain "clean" STEM-WBDF images. Without an objective aperture in the STEM-WBDF method, an ADF detector may receive multiple non-systematic diffraction beams. TEM calculations and experiments have demonstrated that the dislocation images would be altered if non-systematic diffraction beams are contributed to the resultant image (Häussermann, et al., 1973; Sandström, et al., 1974). As shown in Fig. 3k, dark-contrast loops at the top of the image were formed with signals from the direct beam T, whereas bright-contrast loops at the bottom primarily originate from the 2g beam signal. Although the middle region of Fig. 3k appeared to be defect-free, other images revealed the presence of loops in this region. Loops in the middle region were invisible or “canceled” out because the ADF detector detected signals from both the

direct beam T and the 2g beam. This suggests that when multiple beams hit one detector simultaneously, some information can be lost. Therefore, it is advisable for the operator to align the microscope properly and confirm the optic axis, CBED pattern, objective aperture, and BF/ADF detectors are all in the desired position before recording STEM-WBDF images. As a setup verification example (Fig. 4), when employing an optimal configuration of STEM-WBDF method 1, the g disc is covered by the objective aperture. The objective aperture should effectively block all diffracted and direct beams, excluding the g beam. Consequently, no signal can be collected by the STEM-BF detector (Figs. 4c and 4d).

### 4.2 Achieving Improved Resolution of Dislocation Lines in WBDF Conditions

As shown in Figs. 3-6, STEM-WBDF is a superior technique for imaging finer details of dislocations loops. To achieve a significant reduction in the half-width (thickness of the dislocation line), the excitation error of the g beam must be sufficiently large. The criteria for optimal WBDF condition are met with (Cockayne, 1973):

(i) $|s_g \xi_g| \geq 5$

(ii) $|s_g| \geq 0.2$ nm$^{-1}$

(iii) No other spots are strongly excited.

where $s_g$ and $\xi_g$ are the excitation error and the extinction distance of the diffraction beam g, respectively. Cockayne (Cockayne, 1973) established these conditions in TEMs at 100kV, and calculations demonstrated validity at higher voltages (Sandström, 1973). Cockayne proposed two WBDF setups: (1) exciting a higher-order g spot, such as (g, 3g), or (2) a lower-order negative g spot, such as (-g, g). Typically, TEM operators more commonly choose condition (1) with positive n likely because it intuitively aligns with the requirement that $|s_g| \geq 0.2$ nm$^{-1}$. Based on weak beam microscopy theory (Williams & Carter, 2009) and lattice parameters in the Inorganic

Crystal Structure Database (ICSD) (Hellenbrandt, 2004), Table 3 and Table 4 list the $|s_g|$ = 0.2 $nm^{-1}$ condition for several materials with different g vectors with accelerating voltages of 200 kV and 300 kV. Here, n and -n refers to the values where the Ewald sphere intersects. From Table 3 and Table 4, two conclusions could be drawn: (1) for the same absolute value of $s$, the sum of positive n and negative n is 2, irrespective of the chosen excitation error. (2) Compared to WBDF with positive g, achieving WBDF with negative g of the same magnitude of s is easier and has a lower likelihood of exciting other non-systematic diffraction spots. In other words, for the ideal WBDF condition with the narrowest dislocation lines, (g, 3g) may not always be the best condition.

**Table 3.** The value of n and -n for (g, ng) WBDF imaging conditions that reach $|s_g|$ =0.2 $nm^{-1}$ for several BCC materials

| The g spot for imaging | 200kV | | | 300kV | | |
|---|---|---|---|---|---|---|
| | α-Fe | Mo* | V* | α-Fe | Mo* | V* |
| 110 | 7.6 / -5.6 | 8.9 / -6.9 | 9.6 / -7.6 | 9.4 / -7.4 | 11 / -9 | 11.9 / -9.9 |
| 200 | 4.3 / -2.3 | 4.9 / -2.9 | 5.3 / -3.3 | 5.2 / -3.2 | 6 / -4 | 6.5 / -4.5 |
| 211 | 3.2 / -1.2 | 3.6 / -1.6 | 3.9 / -1.9 | 3.8 / -1.8 | 4.3 / -2.3 | 4.6 / -2.6 |

* The condition for BCC W is similar to the one for Mo and the condition for BCC Ta is similar to the one for V.

**Table 4.** The value of n and -n for (g, ng) WBDF imaging conditions that reach $|s_g|$ =0.2 $nm^{-1}$ for several FCC materials

| The g spot for imaging | 200kV | | | 300kV | | |
|---|---|---|---|---|---|---|
| | Ni | Cu | γ-Fe | Ni | Cu | γ-Fe |
| 111 | 7.6 / -5.6 | 7.9 / -5.9 | 8.1 / -6.1 | 9.4 / -7.4 | 9.8 / -7.8 | 10 / -8 |
| 200 | 5.9 / -3.9 | 6.2 / -4.2 | 6.3 / -4.3 | 7.3 / -5.3 | 7.6 / -5.6 | 7.8 / -5.8 |
| 220 | 3.5 / -1.5 | 3.6 / -1.6 | 3.7 / -1.7 | 4.1 / -2.1 | 4.3 / -2.3 | 4.4 / -2.4 |

### 4.3 Recommendations and Potential Applications

The STEM-WBDF method 3 proposed in this study was inspired by Cockayne's negative n WBDF setup (Cockayne, 1973). As shown in Fig. 7, both the (g, 3g) and (-g, g) conditions for STEM-WBDF (Figs. 7c and 7d) yielded similar results with narrower dislocation lines compared to the images acquired under a two-beam condition (Figs. 7a and 7b). In Fig. 3, all three variants of STEM-WBDF methods presented similar and optimal WBDF images. Among these methods, the (-ng, g) condition (see STEM-WBDF method 3 in Table 1.) may be considered to be a more efficient method with a lower likelihood of error, as it generally requires less sample tilting compared to the setup of the (g, ng) condition. Note that in STEM mode, unlike TEM mode, deflecting the direct beam to meet the Bragg condition for WBDF imaging is not possible. The STEM-WBDF method 2 (see Table 1) is simply shifting the CBED pattern with the projection system without affecting the excitation of a specific g disc, unlike the beam deflect (or beam tilt) in TEM mode.

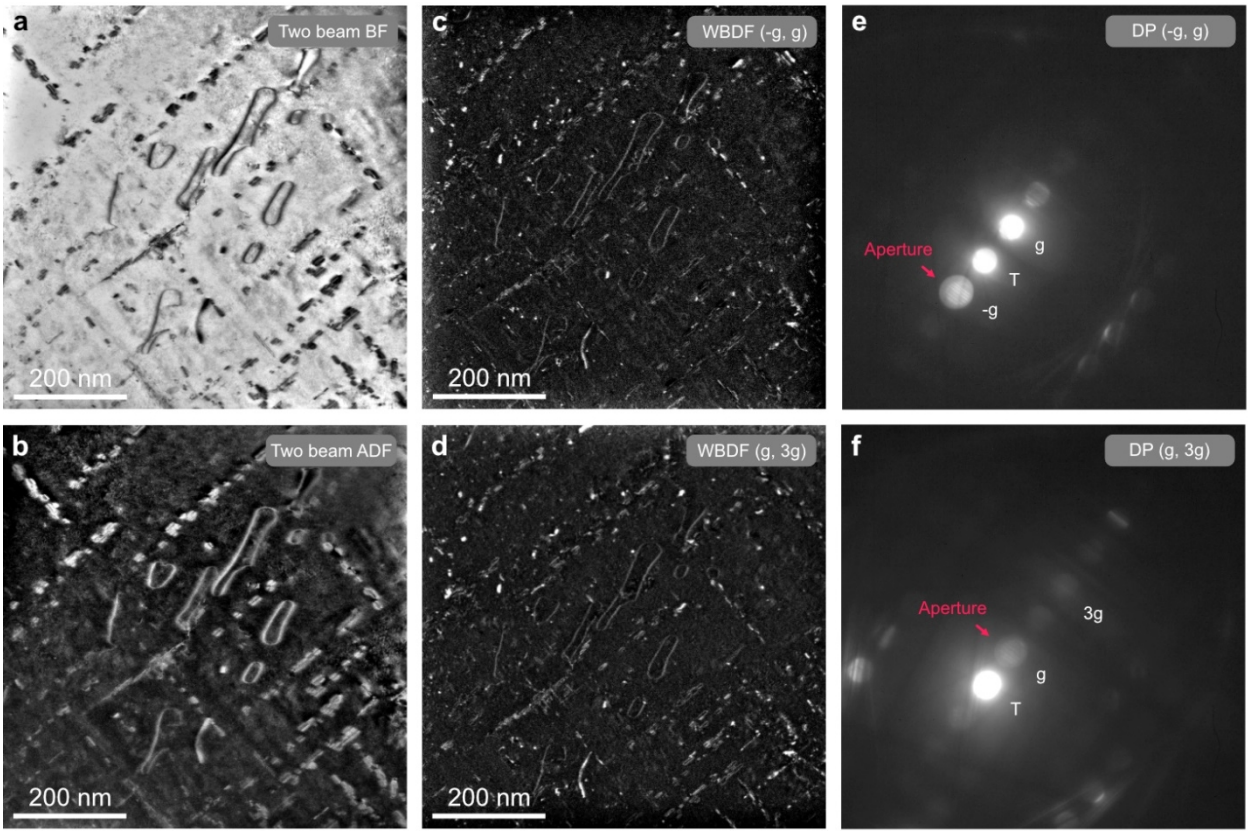


**Fig 7.** Comparison of dislocation thickness in two beam and STEM-WBDF conditions with $g = [110]$: (a-b) two beam condition, (c) STEM-WBDF (-g, g) condition, (d) STEM-WBDF (g, 3g) (e-f) corresponding CBED patterns for the WBDF images.

In addition to the advantages for using STEM for defect analysis, employing STEM-WBDF methods for dislocation loop analysis provides an effective means to isolate defect information efficiently, ensuring a clearer understanding of dislocation loop types. Furthermore, these methods produce narrow dislocation lines, enabling in-depth analysis of small loops, and permit inside-out contrast analysis for precise identification of dislocation loop nature. The STEM-WBDF methods can be used not only to improve dislocation loop imaging but also to analyze dislocation lines in various material systems. Any dislocation analysis conducted using the WBDF method in TEM mode in the past can take advantage of the STEM-WBDF methods. For example, the Burgers vector can be determined for dislocation types such as perfect,

Shockley partial, or Frank partial dislocations. It is necessary to perform a full $g \cdot b$ analysis to determine the Burgers vector of defects, as well as conduct slip trace analysis across other zone axes to identify the slip plane. Additionally, by extending the concept of using objective apertures to select signals from specific g discs in STEM mode, precipitate analysis, such as for centered-dark field (CDF) conditions (Spadotto, et al., 2020), may also derive potential benefit when selecting precipitate or superlattice reflections for imaging.

STEM mode also offers direct accessibility when combined with energy-dispersive X-ray spectroscopy (EDXS) and electron energy loss spectroscopy (EELS) techniques, enabling elemental or thickness mapping within the same imaging area. This integrated approach provides a detailed understanding of solute segregation or element enrichment near or on the dislocations. However, when conducting STEM-EDXS or EELS analyses on specimens oriented along major crystallographic zone axes, it is necessary to consider electron-channeling effects, which can affect electron-induced x-ray emission (Taftø & Spence, 1982) and the intensity of the incident electron wave (Taftø & Krivanek, 1982). In addition, the synergy between STEM defect analysis techniques and 4D-STEM strain mapping techniques (Yu, et al., 2024; Zeltmann, et al., 2019) can be beneficial for studying the strain field of the defects. By combining these approaches, valuable information related to the defects can be obtained, providing a more comprehensive understanding of the crystalline material's behavior under various conditions.

## 5 Conclusions

Employing STEM for defect analysis offers numerous advantages, with the added benefit of suppressing dynamical diffraction contributions to background contrast in the image. Moreover, STEM mode imaging can be executed along zone axes. However, it is essential to

acknowledge potential limitations, such as the possibility of "dirty" STEM-BF or ADF images resulting from using two-beam conditions without an aperture or overlapping CBED discs. Additionally, on-zone STEM imaging may be limited when the defect diameter is less than 10 nm. This study introduces STEM-WBDF methods, which aim to address these challenges and extend the advantages of STEM for defect analysis. These methods enable the isolation of defect information to identify the dislocation loop type, showcasing narrow dislocation lines for small loop analysis, and providing inside-out contrasts to identify the dislocation loop nature. Furthermore, as analytical electron microscopes combine TEM and STEM with EDXS and/or EELS, elemental analysis and/or thickness mapping can be performed within the same STEM imaging area. Moreover, combining STEM defect analysis methods with 4D-STEM techniques allows for obtaining strain mapping information of defects. This holistic approach enhances the depth and precision of defect analysis in materials science.

**Acknowledgments**

We thank Drs. Raymond R. Unocic (ORNL), Lawrence Allard (ORNL), Chad Parish (ORNL), Gerd Duscher (UTK), and Vincent Hou (TSMC) for their insightful comments and suggestions.

**Financial support**

This research was sponsored by the Laboratory Directed Research and Development Program of Oak Ridge National Laboratory (MGB and YRL), and the Office of Fusion Energy Sciences, U.S. Department of Energy (YRL) under contract DE-AC05-00OR22725 with UT-Battelle, LLC. Support was also provided by the Office of Fusion Energy Sciences from grant # DE-SC0023293 with the University of Tennessee (YL&SJZ).

**References**


CHEN, W.-Y., MIAO, Y., GAN, J., OKUNIEWSKI, M.A., MALOY, S.A. & STUBBINS, J.F. (2016). Neutron irradiation effects in Fe and Fe-Cr at 300 °C. Acta Materialia **111**, 407-416.

COCKAYNE, D.J.H. (1973). The principles and practice of the weak-beam method of electron microscopy. Journal of Microscopy **98**(2), 116-134.

FÖLL, H. & WILKENS, M. (1975). A simple method for the analysis of dislocation loops by means of the inside-outside contrast on transmission electron micrographs. physica status solidi (a) **31**(2), 519-524.

FUNG, K.Y., LIN, Y.R., YU, P.J., KAI, J.J. & HU, A. (2018). Microscopic origin of black spot defect swelling in single crystal 3C-SiC. Journal of Nuclear Materials **508**, 292-298.

HALEY, J.C., BRIGGS, S.A., EDMONDSON, P.D., SRIDHARAN, K., ROBERTS, S.G., LOZANO-PEREZ, S. & FIELD, K.G. (2017). Dislocation loop evolution during in-situ ion irradiation of model FeCrAl alloys. Acta Materialia **136**, 390-401.

HÄUSSERMANN, F., KATERBAU, K.H., RÜHLE, M. & WILKENS, M. (1973). Calculations and observations of the weak-beam contrast of small lattice defects. Journal of Microscopy **98**(2), 135-154.

HEIDENREICH, R.D. (2004). Electron Microscope and Diffraction Study of Metal Crystal Textures by Means of Thin Sections. Journal of Applied Physics **20**(10), 993-1010.

HELLENBRANDT, M. (2004). The inorganic crystal structure database (ICSD) - present and future. Crystallography Reviews **10**(1), 17-22.

HERNÁNDEZ-MAYORAL, M., HEINTZE, C. & OÑORBE, E. (2016). Transmission electron microscopy investigation of the microstructure of Fe–Cr alloys induced by neutron and ion irradiation at 300 °C. Journal of Nuclear Materials **474**, 88-98.

HIRSCH, P.B. & WHELAN, M.J. (1960). A kinematical theory of diffraction contrast of electron transmission microscope images of dislocations and other defects. Philosophical Transactions of the Royal Society of London. Series A, Mathematical and Physical Sciences **252**(1017), 499-529.

HOWIE, A., WHELAN, M.J. & MOTT, N.F. (1962). Diffraction contrast of electron microscope images of crystal lattice defects. III. Results and experimental confirmation of the dynamical theory of dislocation image contrast. Proceedings of the Royal Society of London. Series A. Mathematical and Physical Sciences **267**(1329), 206-230.

HUMPHREYS, C.J. (1981). Fundamental concepts of stem imaging. Ultramicroscopy **7**(1), 7-12.

IWATA, H. & SAKA, H. (2017). Resolving individual Shockley partials of a dissociated dislocation by STEM. Philosophical Magazine Letters **97**(2), 74-81.

JENKINS, M.L. (1994). Characterisation of radiation-damage microstructures by TEM. Journal of Nuclear Materials **216**, 124-156.

KLUEH, R.L., SHIBA, K. & SOKOLOV, M.A. (2008). Embrittlement of irradiated ferritic/martensitic steels in the absence of irradiation hardening. Journal of Nuclear Materials **377**(3), 427-437.

LI, Y., SONG, M., ZHU, P., LIN, Y.-R., QI, Z., ZHAO, Y., LEVINE, S. & ZINKLE, S.J. (2023). Flash electropolishing of BCC Fe and Fe-based alloys. Journal of Nuclear Materials **586**, 154672.

LIN, Y.-R., CHEN, W.-Y., LI, M., HENRY, J. & ZINKLE, S.J. (2021). Dynamic observation of dual-beam irradiated Fe and Fe-10Cr alloys at 435 °C. Acta Materialia **209**, 116793.

LIN, Y.R., HO, C.Y., HSIEH, C.Y., CHANG, M.T., LO, S.C., CHEN, F.R. & KAI, J.J. (2014). Atomic configuration of irradiation-induced planar defects in 3C-SiC. Applied Physics Letters **104**(12).

LIU, J. (2021). Advances and Applications of Atomic-Resolution Scanning Transmission Electron Microscopy. Microscopy and Microanalysis **27**(5), 943-995.

MAHER, D.M. & JOY, D.C. (1976). The formation and interpretation of defect images from crystalline materials in a scanning transmission electron microscope. Ultramicroscopy **1**(3), 239-253.

MIAO, J., SINGH, S., TESSMER, J., SHIH, M., GHAZISAEIDI, M., DEGRAEF, M. & MILLS, M.J. (2018). Dislocation Characterization using Weak Beam Dark Field STEM Imaging. Microscopy and Microanalysis **24**(S1), 2202-2203.

PARISH, C.M., FIELD, K.G., CERTAIN, A.G. & WHARRY, J.P. (2015). Application of STEM characterization for investigating radiation effects in BCC Fe-based alloys. Journal of Materials Research **30**(9), 1275-1289.

PHILLIPS, P.J., BRANDES, M.C., MILLS, M.J. & DE GRAEF, M. (2011a). Diffraction contrast STEM of dislocations: Imaging and simulations. Ultramicroscopy **111**(9), 1483-1487.

PHILLIPS, P.J., MILLS, M.J. & DE GRAEF, M. (2011b). Systematic row and zone axis STEM defect image simulations. Philosophical Magazine **91**(16), 2081-2101.

SANDSTRÖM, R. (1973). The weak-beam method in electron microscopy. physica status solidi (a) **19**(1), 83-91.

SANDSTRÖM, R., MELANDER, A. & ERIKSSON, L. (1974). Influence of non-systematic reflexions on weak-beam and high-resolution bright-field images in high-voltage electron microscopy. physica status solidi (a) **26**(1), 273-284.

SPADOTTO, J.C., BURKE, M.G. & SOLÓRZANO, I.G. (2020). On the morphology of grain boundary discontinuous reactions and phase identification in an advanced Cr–Fe–Ni alloy. Journal of Materials Science **55**(23), 10221-10241.

TAFTØ, J. & KRIVANEK, O.L. (1982). Site-Specific Valence Determination by Electron Energy-Loss Spectroscopy. Physical Review Letters **48**(8), 560-563.

TAFTØ, J. & SPENCE, J.C.H. (1982). Atomic site determination using the channeling effect in electron-induced x-ray emission. Ultramicroscopy **9**(3), 243-247.

WANG, Z.L. & BENTLEY, J. (1991). Z-contrast imaging of bulk crystal surfaces in scanning reflection electron microscopy. Ultramicroscopy **37**(1), 39-49.

WEN, M., GHONIEM *, N.M. & SINGH, B.N. (2005). Dislocation decoration and raft formation in irradiated materials. Philosophical Magazine **85**(22), 2561-2580.

WILLIAMS, D.B. & CARTER, C.B. (2009). *Transmission Electron Microscopy: A Textbook for Materials Science*. Springer.

XIU, P., BEI, H., ZHANG, Y., WANG, L. & FIELD, K.G. (2021). STEM Characterization of Dislocation Loops in Irradiated FCC Alloys. Journal of Nuclear Materials **544**, 152658.

YAO, B., EDWARDS, D.J. & KURTZ, R.J. (2013). TEM characterization of dislocation loops in irradiated bcc Fe-based steels. Journal of Nuclear Materials **434**(1), 402-410.

YAO, Z., JENKINS, M.L., HERNÁNDEZ-MAYORAL, M. & KIRK, M.A. (2010). The temperature dependence of heavy-ion damage in iron: A microstructural transition at elevated temperatures. Philosophical Magazine **90**(35-36), 4623-4634.

YU, Z., LIN, Y.-R., ZACHMAN, M., ZINKLE, S. & XU, H. (2024). The Role of Stacking Fault Tetrahedra (SFTs) on Void Swelling in Irradiated Copper. Communications Materials, under review.

ZELTMANN, S.E., MÜLLER, A., BUSTILLO, K.C., SAVITZKY, B.H., MINOR, A.M. & OPHUS, C. (2019). Improved 4D-STEM Strain Mapping Precision Using Patterned Probes. Microscopy and Microanalysis **25**(S2), 1958-1959.

ZHONG, X., ZHOU, X., HAIGH, S.J., WITHERS, P.J. & BURKE, M.G. (2022). Challenges in FIB TEM Sample Preparation: Damage Issues and Solutions. Microscopy and Microanalysis **28**(S1), 60-62.

ZHU, P., ZHAO, Y., LIN, Y.-R., HENRY, J. & ZINKLE, S.J. (2024). Defect-specific strength factors and superposition model for predicting strengthening of ion irradiated Fe18Cr alloy. Journal of Nuclear Materials **588**, 154823.

ZHU, Y., OPHUS, C., TOLOCZKO, M.B. & EDWARDS, D.J. (2018). Towards bend-contour-free dislocation imaging via diffraction contrast STEM. Ultramicroscopy **193**, 12-23.

ZINKLE, S.J. (2020). 1.04 - Radiation-Induced Effects on Microstructure☆. In *Comprehensive Nuclear Materials (Second Edition)*, Konings, R. J. M. and Stoller, R. E. (Eds.), pp. 91-129. Oxford: Elsevier.